Contribution of Swirl Recovery to the Induced Drag of a Propeller-Wing System – A Parametric Study

Nederlof, R.; Kooij, R.N.F.; Veldhuis, L.L.M.; Sinnige, T.

DOI
10.2514/6.2023-3543

Publication date
2023

Document Version
Final published version

Published in
AIAA AVIATION 2023 Forum

AIAA AVIATION Forum
12-16 June 2023, San Diego, CA and Online
AIAA AVIATION 2023 Forum

10.2514/6.2023-3543

Contribution of Swirl Recovery to the Induced Drag of a Propeller-Wing System – A Parametric Study

Robert Nederlof*, Robert Kooij†, Leo L. M. Veldhuis‡, and Tomas Sinnige§
Delft University of Technology, 2629 HS, Delft, The Netherlands

With the rise of distributed propeller concepts, there is an increased interest in quantifying the interaction between propeller slipstream and wing. It is known from literature that the local upwash induced by the propeller swirl can lead to a reduction of the wing-induced drag, a phenomenon often referred to as swirl recovery. However, at the same time, the distortion of the lift distribution due to the slipstream interaction cancels part of the swirl recovery benefit. These two separate mechanisms are often grouped together, but their relative contribution to the change in induced drag of a propeller-wing system is unknown. The goal of this paper is to separate the two mechanisms and to quantify their relative importance in terms of the induced drag of a wing immersed in a propeller slipstream. To this end, an improved approach for fast low-order modeling of the interaction between propeller and wing was implemented. The propeller performance is calculated using a BEM model, after which the induced velocities in the slipstream are modeled using a slipstream tube model. The propeller-induced velocities then have been implemented into a vortex-lattice analysis of the wing, including an often overlooked correction for the finite slipstream height experienced by the wing sections immersed in the propeller slipstream. It was found that the tip-mounted configuration with an inboard-up rotating propeller showed the largest reduction in total induced drag, even though the spanwise lift distribution was disturbed the most compared to other spanwise propeller positions. The swirl-induced drag mechanism outweighs the trailing vortex-induced drag mechanism. This is also true when the propeller is rotating in the other direction, when the largest performance degradation is obtained for the tip-mounted configuration.

Nomenclature

B	=	number of propeller blades	[-]	q	=	dynamic pressure	[Pa]
b	=	wing span	[m]	r	=	resultant force	[N/m]
C_D	=	3D drag coefficient	[-]	T	=	thrust force	[N]
C_d	=	sectional drag coefficient	[-]	T_C	=	thrust coefficient ($T/(\rho V_\infty^2 D_\mathrm{p}^2)$)	[-]
C_L	=	3D lift coefficient	[-]	V	=	velocity	[m/s]
C_l	=	sectional lift coefficient	[-]	v	=	propeller-induced velocity	[m/s]
C_X	=	net-axial force coefficient	[-]	W	=	downwash AIC matrix	[-]
c	=	chord	[m]	w	=	trailing vortex-induced downwash	[m/s]
D	=	drag force	[N]	X	=	axial/streamwise coordinate	[m]
D_p	=	propeller diameter	[m]	Y	=	spanwise coordinate	[m]
d	=	sectional drag	[N/m]	Z	=	vertical coordinate	[m]
F	=	Aerodynamic Influence Coefficients	[-]	α	=	angle of attack	[°]
G	=	aerodynamic correction matrix	[-]	Γ	=	circulation	[m^2/s]
J	=	propeller advance ratio ($V_\infty/(nD_\mathrm{p})$)	[-]	η_p	=	propeller efficiency	[-]
L	=	lift force	[N]	λ	=	taper ratio	[-]
l	=	sectional lift	[N/m]	ρ	=	radial coordinate	[m]
n	=	propeller rotational speed	[Hz]	ρ_∞	=	air density	[kg/m^3]
P	=	reference point in the slipstream	[-]	φ	=	circumferential propeller position	[°]

*PhD student, Flight Performance and Propulsion Section, Faculty of Aerospace Engineering, Kluyverweg 1; Member AIAA. R.Nederlof-1@tudelft.nl
†MSc graduate, Flight Performance and Propulsion Section, Faculty of Aerospace Engineering, Kluyverweg 1.
‡Full professor, Head of Flight Performance and Propulsion Section, Faculty of Aerospace Engineering, Kluyverweg 1; Member AIAA.
§Assistant professor, Flight Performance and Propulsion Section, Faculty of Aerospace Engineering, Kluyverweg 1; Member AIAA.

Subscripts

a	=	axial	n	=	normal
b	=	bound	p	=	propeller
eff	=	effective	s	=	swirl-induced
g	=	geometric	t	=	tangential
i	=	induced	v	=	vortex-induced
j	=	panel index	∞	=	free stream

I. Introduction

Increasing concerns about the environmental impact of air transportation have recently led to a strong drive for more sustainable aviation. Combined with the surge in interest in the so-called personal-air-mobility market, this has resulted in various design and development studies of aircraft with distributed electric propulsion systems. Electric aircraft can reduce the environmental impact of aviation by eliminating emissions and reducing noise in urban environments near airports. Electric motors are practically scale-free, permitting the distribution of multiple small propulsors over the aircraft. This enables performance and noise benefits over conventional aircraft. The limited energy density of batteries, however, imposes that electric aircraft may only become feasible if a beneficial coupling between propulsors and airframe can be exploited to improve the system efficiency even further. Similar to electric cars, energy can be regenerated during flight to reduce energy consumption [1, 2] Furthermore, propellers could be used in negative thrust mode to e.g. improve control authority and more flexible approach trajectories. However, the use of propellers in non-conventional ways will further impact the propeller-wing interaction. For a propeller at negative thrust conditions, the slipstream velocities will be opposite compared to the conventional propeller slipstream [3]. The reduction in axial velocity and the opposite swirl direction could reduce the wing performance. Especially when the propeller-wing system is optimized to maximize the beneficial propulsion integration, using the propellers in non-conventional ways could lead to large performance degradation, hence the importance of understanding the aerodynamic interaction between the propeller(s) and wing can be emphasized.

As discussed in the reference work by Veldhuis [4], the time-averaged interaction for tractor propeller-wing configurations consists of an upstream and downstream effect, affecting both propeller and wing loading. The upstream interaction can be considered equivalent to a modified effective angle of attack of the propeller, while the dominant downstream interaction is due to the increased axial velocity and nonzero swirl in the propeller slipstream for a positive thrust propeller. The study described in this paper will focus on the latter interaction. Early studies [5, 6] on propeller-wing interactions have shown that performance improvements such as lift augmentation and drag reduction are obtained when propellers are integrated cleverly with the wing. The lift augmentation is often attributed to the blowing effect that the propeller(s) have on the main wing. However, the swirl in the propeller slipstream also has a significant influence on the spanwise lift distribution. The drag reduction of propeller-wing systems is achieved by lowering the induced drag of the wing, which is especially happening for wing-tip mounted propeller configuration [7, 8]. The induced drag of a propeller-wing system follows from vertical induced velocities in front of the wing, tilting the resultant force vector at each spanwise segment. Note that the word 'lift' is intentionally omitted compared to the conventional term lift-induced drag. This is because the vertical velocity component at wing segments inside the propeller slipstream is not just determined by the change in circulation (lift), but the swirl velocity of the propeller is added to it. The segments that experience the upwash from the propeller, exhibit a negative induced drag component (in the thrust direction), which is opposite to the conventional lift-induced drag. This phenomenon is called swirl recovery since part of the propeller swirl is recovered in the form of a thrust component.

However, the initial distortion in lift distribution due to the propeller-wing interaction will increase the downwash due to the shed vorticity behind the wing which increases the induced drag again. In most propeller-wing studies, there is only the consideration of the total lift-induced drag, which is the sum of these two mechanisms, and the relative importance of the two is unknown. Therefore, in this research, the total induced drag of the wing is decomposed into the relative contribution of the drag due to the vertical velocity component caused by the shed vorticity, and the drag component caused by the vertical velocity component due to the propeller. To be able to make this distinction, a low-order numerical model was constructed based on potential flow methods. Furthermore, the numerical tool allows for fast evaluation, meaning many different system parameters can be changed. By varying the spanwise position of the propeller, general trends can be observed for the change in induced drag in terms of the two separate mechanisms.

II. Propeller-Wing Interactions & Swirl Recovery

A. Lift Modification

The axial and tangential velocity components induced by the propeller cause separate effects on the spanwise loading distribution. The two effects are visualized in Fig. 1, where it was assumed that the propeller was located somewhere along the semi-span of the wing. Note that only one-half of the wing lift distribution is shown. For a propeller operating at positive thrust conditions, the axial velocity increment inside the slipstream will increase the wing lift due to the increased dynamic pressure. This can be seen in Fig. 1a. The effects of the tangential flow on the C_l-distribution of the wing are visualized in Fig. 1b. There will be an increase in wing loading at the up-going blade side due to the induced upwash component and a decrease in wing loading at the down-going blade side due to the increased downwash.

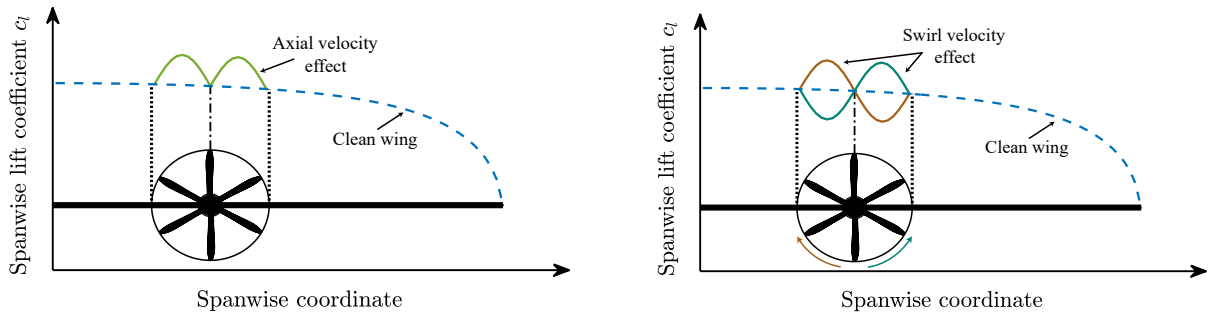

a) Isolated effect of the axial velocity increment inside the slipstream

b) Isolated effect of the swirl velocity inside the slipstream depending on the rotation direction

Fig. 1 Schematic overview of the individual propeller slipstream effects on the wing lift distribution

The effects due to the axial and tangential velocity cannot just be superimposed. The sudden increase or decrease in lift at the slipstream boundary creates strong trailing vortices. These vortices will also influence the surrounding regions. So, the lift of the wing segments not directly submerged in the slipstream is also affected, which in its turn changes the trailing vortex sheet. This means that the whole lift distribution over the entire span is changed and that the initially large peaks are more spread out, see Fig. 2. If the propeller is located away from the tips, the increase in lift due to the increased axial velocity will offset the decrease in lift due to the increased downwash at the down-going blade side, often leading to a net increase in lift for the wing [4]. Note that the described interaction phenomena are valid for a propeller that creates positive thrust. A propeller that is operated in negative thrust and power mode will yield inverted interactions. The axial velocity deficit in the slipstream will then lead to a lift reduction. The negative torque on the propeller blades will mean that the swirl induced by the propeller is in the opposite direction compared to the propulsive case, and hence the up- and downwash regions are swapped.

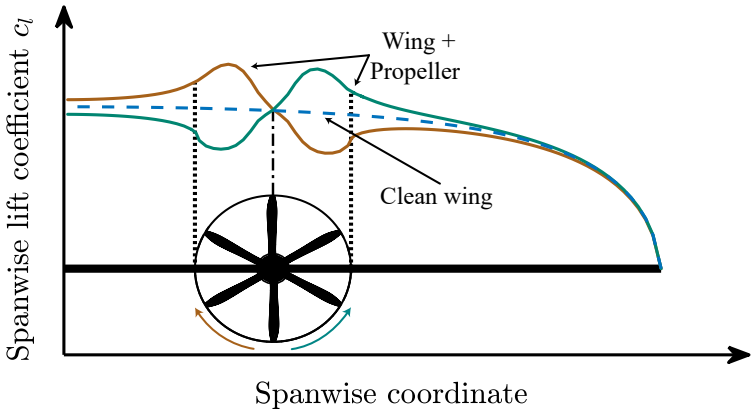

Fig. 2 Schematic overview of the integral effect of the propeller induced axial and tangential velocity on the wing's spanwise lift distribution

B. Drag Modification

Often, only the lift component is considered in the analysis of propeller-wing interactions. However, the drag of the wing will also be altered by the propeller slipstream interaction. For the total drag of the wing, two main components can be distinguished, namely the profile drag and the (lift-)induced drag. The former is a consequence of the viscous interaction of the air with the wing and is mainly driven by the 2D airfoil shape and the inflow conditions (e.g. Reynolds number). It is formed by the combination of the pressure drag and the skin-friction drag. The induced drag is an inviscid effect and a consequence of the changed inflow conditions at the wing segments. However, in high-fidelity analyses, the term pressure drag includes the vortex-induced drag phenomenon since the inviscid effects cannot be split from the viscous effects. In this study, the focus is put on the induced drag component.

1. Clean Wing Induced drag

For any 3D wing, there will be a vertical velocity component at each spanwise segment, caused by the downwash (w) produced by the trailing vortex sheet, see Fig. 3. The shed vorticity is a function of the spanwise gradient of the circulation distribution and hence the induced drag is a function of the shape of the circulation distribution over the wing. The lift and circulation are closely related and the term lift-induced drag is often used since this drag component is a direct consequence of producing lift on a three-dimensional wing. The negative induced angle of attack (α_i) caused by the downwash of the trailing vortex sheet will slightly reduce the resultant force vector (r), but more importantly, will tilt it backward. Note that in this visualization, the profile drag is omitted for clarity, hence the resultant force is equivalent to the lift force for undisturbed wing sections. The resultant force can then be decomposed into a force perpendicular to the undisturbed free stream (lift (l)) and a component perpendicular to the undistributed free stream (induced drag (d_i)). For small induced angles of attack, the lift is almost equal to the resultant force.

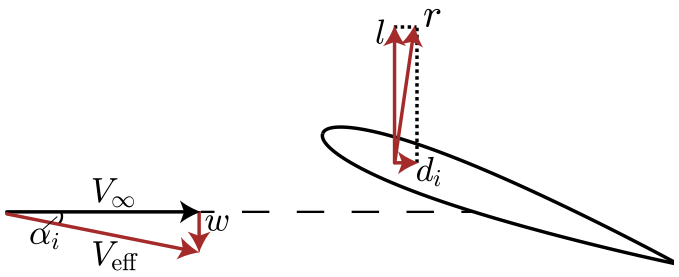

Fig. 3 Schematic overview of the origin of (lift-)induced drag for a conventional wing segment

2. Separate Induced Drag Mechanisms for Propeller-Wing Systems

The interaction of the propeller slipstream with the wing will change both the profile drag and the induced drag. The profile drag is changed due to the change in inflow conditions of each spanwise section inside the propeller slipstream, namely a different dynamic pressure, and a changed inflow angle. This change in drag is not further considered in this paper. The induced drag component for a propeller-wing system is changed in two different ways. Firstly, the change in the circulation distribution due to the induced velocities in the propeller slipstream will mean there are stronger vortices shed in the wake. The more the circulation distribution is disturbed by the slipstream interaction compared to the clean wing (see Fig. 2), the more this increase in downwash will be, even though there might be no net increase in total lift. For the propeller-wing system, the vertical velocity component at the wing segments inside the slipstream does not only depend on the downwash generated by the trailing vortex sheet but also on the swirl velocity in the propeller slipstream. Therefore, the induced drag is also directly influenced by the propeller swirl velocity.

The phenomenon responsible for reducing the overall induced drag is called swirl recovery [4], which is schematically shown in Fig. 4a. Firstly, the free stream velocity (V_∞) is increased by the propeller-induced axial velocity (v_x). Secondly, the vertical velocity component for wing segments inside the slipstream is altered due to the swirl velocity. Note that the velocity and force components are not drawn to scale in Fig. 4. At the wing sections that are behind the up-going blade side, the upwash (v_z) due to the propeller swirl velocity increases the local effective angle of attack. This effective angle of attack is then reduced slightly again by the downwash of the trailing vortex sheet (w), but the induced angle of attack remains positive. This increases the magnitude of the resultant force (away from conditions that would induce flow separation). The resultant force is defined perpendicular to the effective velocity vector (V_{eff}). So the propeller upwash not only increases the local resultant force but also tilts it forward into the direction of the free stream.

This phenomenon is the opposite of the conventional lift-induced drag since the decomposition of the resultant force now results in a component in the forward direction, which is a thrust (negative drag) component. Note that due to the change in lift, the wing-induced downwash component will also be changed, not only for the wing segments inside the slipstream but for all the wing segments. Since the downwash reduces the resulting vertical velocity component caused by the swirl, the term swirl recovery is often used in literature. However, a better name would be swirl reduction, since it is the lost energy in the propeller swirl that is being recovered by the wing in the form of a thrust component.

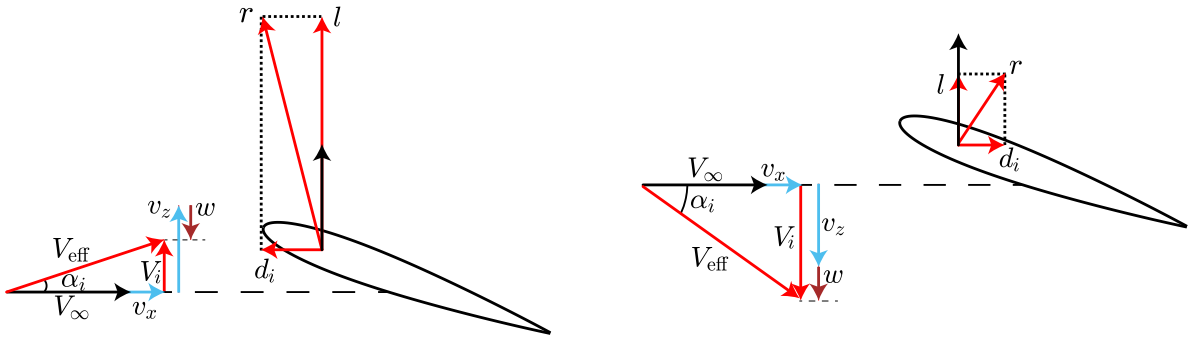

a) Upwash effect at the up-rotating blade side **b) Downwash effect at the down-rotating blade side**

Fig. 4 Schematic overview of the induced vertical velocity effects on the resultant force of the wing sections immersed in a propeller slipstream

At the wing sections behind the down-going blade side, the local effective angle of attack of the wing is increased in the negative sense, resulting in a decrease in the magnitude of the resultant force compared to wing segments without swirl component, see Fig. 4b. The negative induced angle of attack tilts the resultant force vector backward, leading to a positive induced drag. So on this side of the propeller, the swirl adds to the conventional induced drag mechanism for clean wings. When looking at the vertical velocity component (V_i), it could be argued that the swirl velocity is increased with the vortex-induced downwash and hence the swirl recovery (or swirl reduction) here is negative. Just considering this swirl recovery phenomenon inside the slipstream, the net effect of this interaction will be often a thrust component, since the forward tilting happens at the wing sections where the resultant force is increased, whereas the backward tilting happens at the wing sections where the resultant force is reduced. However, this depends on the spanwise lift distribution and the propeller spanwise position. So part of the lost energy from the propeller in the form of a swirling motion is recovered by a net force that reduces the drag of the propeller-wing system. For propeller-wing systems, the change in downwash due to the change in the gradient of the circulation distribution will counteract this net swirl recovery effect. Especially, since the circulation distribution for a propeller-wing system is more disturbed than for the clean wing, the induced drag of sections outside of the slipstream could be increased. In this study, the total induced drag vector of each wing segment is split into the relative contribution of the propeller swirl and the contribution of the downwash induced by the trailing vortex sheet. Therefore, the term induced drag is used instead of lift-induced drag. The induced drag is the sum of the drag caused by the resulting vertical velocity (V_i), consisting of the propeller swirl and the downwash of the trailing vortex sheet. At the up-going blade side, the two will counteract each other, while they add up at the down-going blade side. The changed downwash of the vortex sheet due to the changed loading will affect all the wing segments. In the remainder of this paper, the component of the induced drag caused by the propeller swirl velocity will be referred to as swirl-induced drag. The second component of the (total) induced drag is caused by the downwash of the trailing vortex sheet and will be referred to as vortex-induced drag.

C. Reflection on State-of-the-Art

Lately, there have been multiple studies regarding the wingtip-mounted propeller and its possible wing performance enhancement [9–13]. The tip-mounted propeller that rotates inboard-up has a swirl component that is in the opposite direction of the tip vortex, thereby reducing the net downwash on the wing. This results in a reduction of vortex-induced drag. In a recent study by Sinnige et al., it was found that the drag was reduced by around 15% for moderate lift coefficient and thrust settings [9]. For higher wing loading and thrust setting, the benefit was even higher. Flowfield measurement indeed confirmed the reduction in swirl velocity behind the propeller. The second benefit of a tip-mounted

propeller, as discussed before, is the fact that the wing only operates in the up-going swirl component, since the down-going blade region is outside of the wing region, resulting in a lift increase. However, the wing area over which the axial component washes also is halved, and is characterized by a low loading due to the vicinity of the wingtip. The increase in lift was therefore 1-4% smaller compared to a conventional configuration, where the propeller was positioned on the inboard part of the wing span [9]. Furthermore, placing the propeller closer to the tip disturbs the clean wing lift distribution increasingly, leading to a larger increase in vortex-induced drag, counteracting the large swirl recovery benefit. Therefore, finding the optimal position of the propeller along the wing in terms of overall performance gain in the conceptual design phase is not straightforward. Depending on the propeller geometry, operational conditions, and the wing planform parameters, the performance enhancement is increased or decreased. Even higher performance enhancements were obtained for a tip-mounted configuration in the study from Hooker et al., where the drag of the wing was reduced between 22% and 42% depending on the propeller thrust setting [12].

Most of the optimization studies performed in the past are based on a fixed propeller geometry and position in which it is tried to find the optimal wing shape with that propeller, without changing the propeller position, size, and rotation direction. By fairly comparing all possible different designs in an iterative way, e.g. for a fixed amount of lift and net thrusting force, different conclusions may be drawn for the most optimal layout [14]. Furthermore, the focus is often put on the total change in integral C_L and C_D without focusing on the spanwise distribution of these forces. Possibly, it could be concluded that tip-mounted propellers are not the most efficient design for a specific aircraft mission, especially taking the possible non-conventional use of propellers into account. This was also the conclusion of a recent study by Cole et al.[15], where for the considered configuration, an outboard-up rotating propeller located close to the wing root turned out to be the most efficient layout, which is contrary to most research. Furthermore, it was concluded that the change in lift was almost not altered by varying the design parameters, while the spanwise drag distribution was altered significantly while changing the design [15]. Both the change in spanwise profile drag and total induced drag were investigated individually, concluding that the change in the latter is dominant. However, the induced drag was still considered as a single variable and therefore it could only be hypothesized that the reduction in induced drag was actually due to the more flattened lift distribution, rather than the swirl recovery [15]. This highlights the need for understanding the separate mechanisms behind the modification of the induced drag of the wing caused by the slipstream-wing interference, and how it relates to the total drag of the aircraft.

Depending on the propeller position, rotation direction, and wing planform parameters, there will be a net increase or decrease of the total induced drag due to, on the one hand, the net swirl recovery effect, and on the other hand, the increase in vortex-induced drag due to the disturbance of the circulation distribution. Placing the propeller at a position where the spanwise lift gradient is larger, can lead to a larger net decrease of induced drag, due to the relative big absolute difference in lift between the up-going and down-going blade sides [5, 6]. In the most extreme case, for a tip-mounted propeller, the down-going blade side will be outside of the wing span, maximizing the swirl recovery effect. However, a propeller placed at the tip will also have the greatest disturbance on the lift distribution. Even though there has been an understanding of the propeller placement in the design of propeller-wing systems by reducing the induced drag of the wing, it is not fully understood how the vortex-induced drag and swirl-induced drag (or thrust) contribute to the induced drag of the system. The induced drag has always been considered a single force, whereas the distinction between the two components of the induced drag has not been made. To increase the performance of future propeller-wing systems, this research focuses on the decoupling of and the interaction between vortex-induced drag and swirl-induced drag to investigate their relative contribution to the total induced drag of propeller-wing systems. By optimizing the propeller slipstream-wing interactions, the wing performance increase can significantly aid the overall system efficiency increase needed for new distributed propeller concepts.

Next to the time-averaged effects, the unsteady flowfield of the propeller slipstream also leads to unsteady interactions [16, 17]. Although this is highly relevant for passenger comfort (vibrations and associated interior noise), its effect on overall vehicle performance is limited. Therefore, the present paper only considers the time-averaged performance, ignoring the unsteady phenomena. The strong propeller-wing interactions feature complex flowfields, which make it challenging to accurately model the aerodynamics involved. Therefore, high-fidelity analysis tools such as dedicated wind-tunnel experiments and advanced computational fluid dynamics are required to assess the fundamentals of the interactions. However, such tools are impractical to apply during design studies at aircraft level because of excessive run times and cost. Instead, accurate low-order methods based on potential flow solutions are needed to integrate the performance effects of propeller-wing interactions into preliminary design codes. Furthermore, the use of low-order numerical tools allows for the separate analysis of the two mentioned induced drag mechanisms. Using high-fidelity tools, the total drag can only be split into the pressure drag and the viscous drag component. However, this pressure drag component partially contains the induced drag mechanism, which cannot be separated.

III. Methods

To be able to distinguish the different drag components, a low-order numerical model was created that models both the propeller performance and the wing performance, using vorticity models. The numerical model features the ability to decouple the influence of the wing-induced velocities and the propeller-induced velocities on the aerodynamic performance of the propeller-wing system in terms of drag components. Furthermore, the computational expense of the numerical model is generally low, enabling the analysis of many different propeller-wing system configurations. The numerical model contains three components, namely the propeller, the slipstream, and the wing. Firstly, the modeling of the propeller performance and the resulting induced velocities in the slipstream is discussed in Sec. III.A. The induced velocities of the propeller are then added to the vortex model that is used to calculate the wing performance, see Sec. III.B. In Sec. III.C, the integration of the separate models is discussed and the comparison with experimental data is presented in Sec. III.D.

A. Propeller Performance and Slipstream

To model the propeller performance (thrust and power) and the associated induced velocities in the slipstream, two different models were used. The first model was used to calculate the propeller forces and moments. The calculated circulation distribution on the blades was then used as input for the second model, to be able to calculate the induced velocities at a random point inside the slipstream.

1. Propeller Integral Forces

The performance of the propeller is modeled using an ordinary Blade Element Momentum (BEM) model. The BEM model from Drela [18] was used, which is also widely used for the analysis and design of propellers and rotors in existing codes, such as XROTOR, QPROP, and QMIL. The propeller geometry used was that of the TUD-XPROP propeller, which is representative of a turboprop propeller [19]. Ideally, the geometry of the propeller should also be part of the analysis routine, to maximize overall efficiency. However, to reduce complexity and run time, the propeller geometry was kept fixed in this study. The propeller blade pitch setting and advance ratio were varied to achieve a specific thrust setting while maximizing propeller efficiency. The 2D airfoil polar data was obtained using RFOIL, which includes a correction for the centrifugal pumping effect [20]. The aerodynamic polars were obtained for a large range of Reynolds and Mach numbers, such that these similarity parameters were also taken into account. Prandtl's tip and root loss correction factors were applied to make the model even more accurate. The aerodynamic data was then used to calculate the blade loading for a specific input condition (pitch angle and rotational speed). The BEM model was used to generate a realistic loading condition for the slipstream tube model and hence for the estimation of the slipstream-induced velocities. However, the BEM was used in a one-way interaction only, in other words, the change in propeller loading due to the presence of the wing was not taken into account. Also, the secondary effect, which would be the change in propeller loading due to the change in wing loading (due to the propeller-wing interaction) is not captured by the model. Finally, the BEM model was always used assuming uniform inflow, hence angle of attack effects were not captured.

2. Slipstream Tube Model

To model the interaction effect of the propeller slipstream on the wing aerodynamic performance, the induced velocities inside the slipstream are to be calculated. To model the induced velocity components in the slipstream of the propeller, different models can be used. The induced velocities from the BEM method can already give some insights into the axial and tangential velocity components at the blades and far away from the propeller disk, where the slipstream is fully developed. However, only simple actuator disk methods can be applied to interpolate the BEM values such that the velocities can be known throughout the whole slipstream. To get a more detailed analysis of the slipstream, different types of vortex methods can be used. A propeller lifting-line method, using a fixed wake, can yield more accurate velocities inside the slipstream compared to BEM at relatively low computational cost. More advanced iterative free-wake methods can even further improve the accuracy, but at increasing computational cost. One attractive, and fast, model is the slipstream tube model, which is more or less a time-averaged lifting-line, fixed-wake, model. The slipstream tube model is a relatively simple model which uses panels of distributed vorticity to model the propeller slipstream velocities. The model is described extensively in [4]. A schematic representation is shown in Fig. 5. The total amount of vorticity is split into three different systems. Namely rings of tangential vorticity, cylindrical surfaces of axial vorticity, and the bound vorticity at the propeller blades.

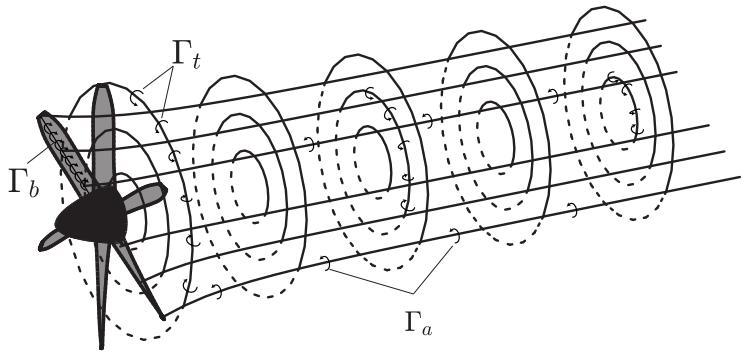

Fig. 5 Schematic representation of the slipstream tube model

The tangential vorticity rings will generate the axial induction inside the slipstream, while the axial vorticity and the bound vorticity contribute together to the swirl velocity component. The three vorticity elements are schematically shown in Fig. 6. In this figure, the propeller disk is located at the $y-z$ plane. The strength of these vorticity components is determined by the blade loading, which can be obtained by using another numerical tool or experimental data. So the slipstream tube model does not model the propeller performance itself, compared to a lifting-line method. By applying the Biot-Savart law, the induced velocity components in a random point inside the slipstream can be calculated. The worked-out slipstream tube model, as described in [4], has some simplification to it since part of the equations was solved analytically, reducing the need for discretization. For example, the slipstream tube has a constant diameter everywhere and hence does not model the contraction or expansion of the slipstream. However, these simplifications were avoided by applying a stepwise method, increasing the accuracy. This stepwise scheme solves the induced velocity by discretizing the tube in the axial direction. By using the induction factors from the BEM model, the contraction can be calculated and hence the rings can be sized to match the proper slipstream in a more realistic manner.

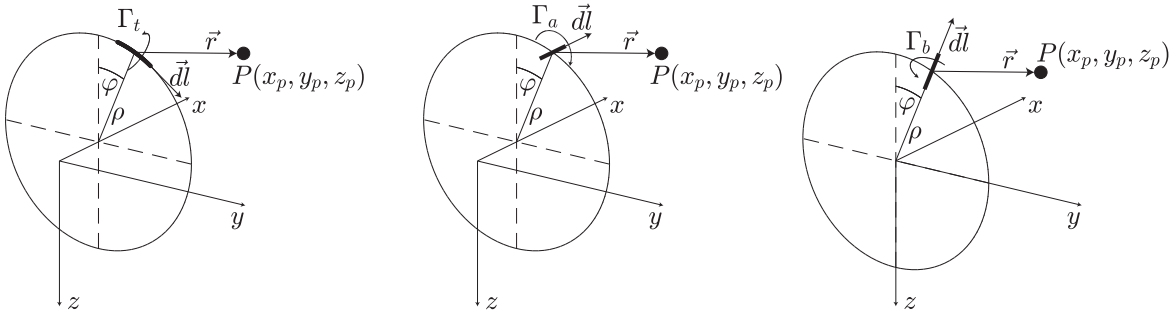

a) Induced velocity due to the tangential vorticity elements

b) Induced velocity due to the axial vorticity elements

c) Induced velocity due to the bound vorticity elements at the blades

Fig. 6 Induced velocity in point *P* due to the three individual slipstream tube vortex filaments (derived from Veldhuis [4])

The strength of the vorticity elements, that determine the induced velocity in a random point P, is determined by the bound circulation of the propeller blades. The axial induction in the slipstream will be generated by rings of distributed tangential vorticity. The strength of the distributed vorticity at a specific radial position (ρ) is a function of the change in the bound circulation of the propeller ($d\Gamma/d\rho$), which is being shed in the slipstream as free (trailing) vortices. Using the BEM method, this bound circulation distribution can be calculated using the Kutta-Joukowski theorem. In theory, infinitely many rings will be placed along the propeller radius and in the streamwise direction. To cover the whole slipstream, rings will be placed in between the propeller plane ($x = 0$) and $x = \infty$ creating cylindrical surfaces. The strength of the tangential distributed vorticity is also a function of the rotational speed (n), the number of blades (B), and the free stream velocity (V_∞). The strength of a tangential vortex filament (Γ_t) is equal to the distributed vorticity over a small width dx, see Fig. 6a, and is given by Eq. 1.

$$\Gamma_t = \frac{nB}{V_\infty}\frac{d\Gamma}{d\rho}dx \tag{1}$$

The swirl velocity in the slipstream is determined by the axial vorticity elements. They are placed on cylindrical surfaces, parallel to the axis of rotation, and perpendicular to the tangential vorticity elements. Again infinitely many cylinders are placed in the radial direction. The strength of the axially distributed vorticity at a specific radial position is equal to the shed circulation in the wake but spread out over the circumference of the cylinder. The strength of an axial vortex filament (Γ_a) is equal to the distributed axial vorticity over the small width of the filament $rd\varphi$, see Fig. 6b, and is given by Eq. 2.

$$\Gamma_a = \frac{B}{2\pi\rho}\frac{d\Gamma}{d\rho}d\rho\rho d\varphi = \frac{B}{2\pi}\frac{d\Gamma}{d\rho}d\rho d\varphi \tag{2}$$

Finally, the bound vorticity of the propeller also will alter the slipstream-induced velocities. The bound vorticity will be concentrated in annuli at the propeller disk. The influence of the bound vorticity will quickly drop as x is increased, but is needed in the calculations such that the swirl velocity jumps instantaneously to the constant value of twice the tangential induction at the blades. The strength of the bound distributed vorticity at a specific radial position is simply that of the value of the bound circulation of all the blades combined, spread out over the circumference. The strength of a bound vortex filament (Γ_b) is equal to the distributed bound vorticity over the small width of the filament $rd\varphi$, see Fig. 6c, and is given by Eq. 3.

$$\Gamma_b = \frac{B}{2\pi\rho}\Gamma\rho d\varphi = \frac{B}{2\pi}\Gamma d\varphi \tag{3}$$

Important to note is that singularities can arise when point P is chosen too close to the vortex sheets control points of the tube. The induced velocities of the propeller at the location of the wing are evaluated precisely in between the vortex sheets of the slipstream tube model, such that singularities are avoided. The slipstream tube model is used as input for the vortex lattice model, which calculates the wing performance. However, the wing-induced velocities are in their turn not taken into account in the development of the slipstream. So this is a shortcoming of the model since the slipstream in reality will deform due to the induced velocities of the wing.

B. Wing Performance

For the modeling of the wing aerodynamic performance, also low-order models are used, based on potential flow theory. Compared to ordinary low-order tools, an additional correction has been applied which prevents an overestimation of the lift augmentation due to the propeller slipstream.

1. Vortex Lattice Method

The lifting-line method is not capable to model wings with small aspect ratios or wings that contain sweep, hence a Vortex Lattice Method (VLM) is used. This is because the influence of the bound vorticity elements is not taken into account, which only works when the quarter chord line is straight [21]. The circulation distribution in the VLM is found by calculating the induced velocity of all panels required to have no velocity component perpendicular to the wing in the control points. In this study, the Weissinger method [22] is applied, which is basically a VLM with a single panel in the chord-wise direction. This reduces the computational cost of the model, while at the same time avoiding the limitations for swept wings. Having only one control point for all the spanwise sections, at the three-quarter chord point, limits the ability to model highly cambered wing sections though. Furthermore, it is assumed that the propeller is aligned with the free stream velocity. A schematic view of the VLM is shown in Fig. 7.

With the flow tangency boundary condition and the Biot-Savart law to find the induced velocities of the vortices, a set of linear equations can be derived. So the sum of all normal velocity (V_n) components must be equal to zero, which is mathematically shown in Eq. 4.

$$V_n = V_{\infty,n} + V_{p,n} + V_{\Gamma,n} = V_\infty \sin\left(\alpha_g\right) + v_x \sin\left(\alpha_g\right) + v_z \cos\left(\alpha_g\right) + \sum_j V_{\Gamma,n_j} = 0 \tag{4}$$

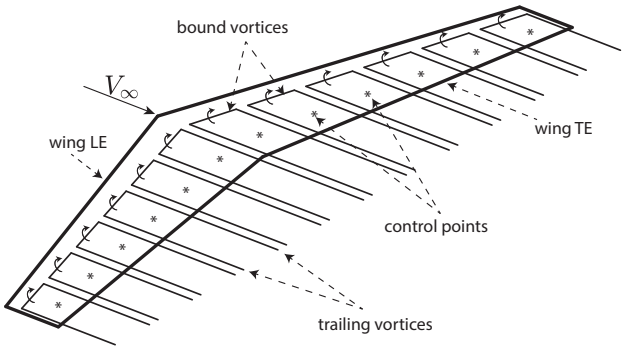

Fig. 7 Single panel (Weissinger) VLM including the control points

So the normal velocity at a control point consists of the free stream normal velocity component, the propeller-induced normal velocity component, and the induced velocity component of the horseshoe vortices of all panels (j) in the normal direction, where α_g is the geometric angle of attack. The propeller-induced velocity components consist of two individual contributions. There is the axial induced velocity (v_x), that is added to the free stream velocity component for spanwise segments that are immersed in the slipstream. The second propeller-induced contribution is the swirl velocity (v_z), normal to the wing. The first three velocity components are model inputs, from which the propeller-induced velocities are given by the slipstream tube model. Using these, the vorticity strength of all panels can be calculated, see Eq. 5. This is done by first calculating the Aerodynamic Influence Coefficient (AIC) matrix ($[F]$), which is determined by the distances from the horseshoe vortices to the control points. What is added to this VLM is a correction to take the effects of the finite slipstream dimensions into account ($[G_F]$) [23]. More detail about this correction is presented in Sec. III.B.2.

$$V_{\Gamma,n} = ([F] + [G_F])\,\Gamma \tag{5}$$

From the resulting bound circulation distribution, the resultant force of each spanwise section can be found using the Kutta-Joukowski theorem, where the local effective velocity of each spanwise segment is used. This means that for the sections immersed in the slipstream, the axial velocity is added to the free stream velocity. The term resultant force is used again, because the force calculated using the Kutta-Joukowski theorem will be perpendicular to the effective velocity, and not the undisturbed free stream velocity. The sectional lift can be calculated using the induced angle of attack, see Eq. 6. The total drag of each spanwise section (d) is then found by calculating the sectional profile drag (d_{pr}) and the induced drag (d_i), see Eq. 7. The former could be calculated in an empirical way, by using drag polars from a 2D solver for example. However, this method would be rather inaccurate considering the lift increase is not just reached by a change in angle of attack, but rather due to the slipstream interaction. Furthermore, this study focuses on the induced drag components, hence the profile drag is left out of consideration. Therefore, the sectional drag is equal to the combined induced drag.

$$l = \cos(\alpha_i)\, r = \cos(\alpha_i)\,(\rho_\infty V_{\text{eff}} \Gamma) \tag{6}$$

$$d = \cancel{d_{pr}} + d_i = \cancel{f(C_l, Re)} - \sin(\alpha_i)\, r \tag{7}$$

The induced drag is calculated by the induced angle of attack (α_i) at each section and multiplying it with the sectional resultant force value. Note that a positive α_i is defined to result in a forward tilting of the resultant force, hence a minus sign is added to make the induced drag a negative value when swirl recovery is present. The combined induced angle of attack can be calculated using the VLM and is then split into the two mechanisms of interest, namely the vortex-induced component, caused by the downwash of the circulation distribution, and the swirl-induced component caused by the propeller swirl. This is mathematically described in Eq. 8, where for each spanwise section, the local velocity is used. w is the downwash generated by the complete vortex system. The AIC for the downwash is denoted by W, which is similar to F, but then for the bound vortex line. Similar to F, a correction is applied to the downwash calculation, such that the limited slipstream height is taken into account (G_W). Note that to increase the accuracy of the method, the induced angle of attack could be calculated by taking the arcsine of the velocity ratios, but the small angle approximation allows for the simplification.

$$\alpha_i = \frac{w}{V_x} + \frac{v_z}{V_x} = \underbrace{\frac{[W - G_W]\,\Gamma}{V_x}}_{\text{vortex induced}} + \underbrace{\frac{v_z}{V_x}}_{\text{swirl induced}} \tag{8}$$

For the vortex-induced drag of the wing, the downwash generated by the trailing vortex system needs to be calculated. This downwash is different from the $V_{\Gamma,n}$ used before since the downwash is the vertical velocity component of all horseshoe vortices induced at the lifting line (bound vortex elements at the quarter chord) itself instead of the control points used for the initial calculation of the circulation distribution. Since the resultant force applies at the bound vortex elements, the vortex-induced downwash needs to be calculated there. Hence, the geometrical point in which circulation-induced velocity must be calculated is shifted upstream compared to the control points that are beings used for the flow tangency condition. Therefore the AIC used before is not correct anymore, and the coefficient matrix $[W]$ is used. The two vertical velocity components are isolated, such that their individual contribution to the induced drag can be analyzed. Note that the conventional vortex-induced downwash is defined as a negative value, resulting in a negative α_i. If the propeller-induced upwash is larger than the vortex-induced downwash, the induced angle of attack will become positive, leading to a negative total induced drag component, meaning an additional thrust component. If the propeller swirl is negative, it adds to the vortex-induced downwash, increasing the induced angle of attack in the negative sense.

2. Correction for the Finite Slipstream Dimensions

The general shortcoming of the VLM is the way the propeller slipstream velocities are included. As shown before in Eq. 4, the velocity components at the control points induced by the propeller are simply added to the free stream velocity. This 2D approach of adding slipstream velocities to the free stream conditions is not fully correct, since it does not include the finite height of the slipstream at each spanwise section [24]. If e.g. there would be a constant axial velocity distribution inside the slipstream, two adjacent spanwise sections would have the same v_x and hence the same lift augmentation. However, the fact that one of the two spanwise sections has a different local slipstream height would change this lift augmentation. In the limiting case of the spanwise section that is located at the edge of the slipstream, where the slipstream height would be very small, the lift augmentation should vanish, irrespective of the possible v_x value. Furthermore, by simply adding the propeller velocities to the free stream, there would be an instantaneous jump in the lift distribution, due to the use of the Kutta-Joukowski theorem, which uses the local velocity and this instantaneous jump is non-physical. Therefore, there is a need for a correction of the VLM system, to get a more accurate modeling of the propeller-wing interaction. The $[G]$ matrix in Eq. 5 is this correction term and is defined using a method from Rethorst [23]. The $[G_W]$ matrix is calculated for the trailing vortex system, such that the downwash calculation is also corrected.

C. Model Integration

The three numerical models were integrated to model the complete propeller-wing system. As mentioned before, the BEM method does not incorporate the angle of attack effects in the propeller performance modeling. The circulation distribution used for the slipstream tube model is therefore also not adjusted for the angle of attack. Therefore, it was chosen that the propeller slipstream is aligned with the free stream. Furthermore, the slipstream tube model is not influenced by the induced velocities of the wing, hence it is modeled to go straight. This means that the propeller and slipstream are decoupled from the wing, where the wing rotates within this system as the angle of attack is varied. A schematic side view of the propeller-wing system is shown in Fig. 8.

Possible twist is added to the geometric angle of attack (α_g). The wing leading edge is placed at a distance x_p from the propeller disk. The propeller-induced velocities u_x and u_z are added to the free stream velocity, and together with the downwash of the trailing vortex sheet, they form the effective velocity vector and hence the induced angle of attack. It should be noted that the propeller-induced velocities are used to analyze the propeller-wing system but that the thrust of the propeller is left out of consideration. In other words, the drag of the wing is not being put equal to the propeller thrust. The control points of the wing panels remain on the same vertical height as the longitudinal axis of the propeller slipstream. This is important as the jet correction assumes that the wing is located in the center of the jet with respect to its height. To realistically represent propeller-wing systems, the angle between the propeller and wing should remain small, which limits the angle of attack. Furthermore, increasing the angle of attack of the wing too much would, in reality, result in flow separation, which is not included in the numerical model based on the potential flow theory.

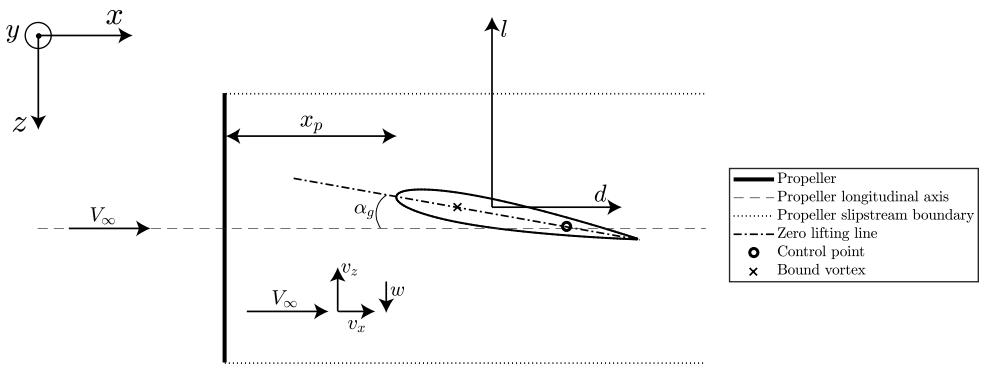

Fig. 8 Side view of the propeller-wing system configuration within the propeller slipstream used for the model integration

D. Comparison with Experimental Data

The individual components of the numerical model have been checked against experimental data in the past and the comparison of these is therefore omitted in this paper. The complete propeller-wing system model results are compared to experimental data obtained by Sinnige et al. [9]. The experimental data consists of forces, which are measured by the external balance to which the propeller-wing system is attached. These measured forces consist not only of the lift, profile drag, and induced drag of the system but also of the viscous drag on the system, and the thrust of the propeller. This means it is difficult to get an estimation of the isolated propeller performance during the experiment. To compare the numerical model with the experiment, an approximation of these two forces of the system had to be made. The friction drag from the propeller-off configuration is included in the configurations analyzed with the numerical model for this comparison. The polars for both the numerical model and the experiment are presented for three different propeller advance ratios in Fig. 9.

As mentioned before, the BEM model does not capture the effects of the inflow angle of attack, while during the experiment, the propeller was fixed to the wing and hence rotated with the angle of attack of the wing. For the purpose of validating the model, the propeller slipstream in the model was adjusted to be aligned with the wing, such that the axial velocity is aligned with the wing chord, as was the case during the experiment. In the BEM, this angle of attack was not modeled, leading to a discrepancy. When considering the propeller thrust, the angle of attack effect would increase its value, and hence the numerical model would under-predict the propeller thrust. The upwash of the wing would also affect the propeller performance, which is not included in the numerical mode. Especially for high wing loading conditions, this effect could cause discrepancies. The setup of the wind tunnel experiment is discussed in detail by Sinnige et al. [9]. The model in that study could be used in twofold, namely as a conventional propeller setup, where the propeller was mounted at $y_p/(b/2) = 0.444$, and a tip-mounted configuration ($y_p/(b/2) = 1$), where the outboard part of the wing of the conventional configuration was removed. The prediction of the numerical model is compared to the results from the experiment for both configurations, such that the effect of the spanwise position of the propeller on the performance of the system is included in the comparison. In the results, the net-axial force coefficient ($C_X = (D - T)/(q_\infty S)$) was used instead of the drag coefficient, since the thrust of the propeller was included in the external balance measurements. Note that the surface area was not the same for the two configurations. Hence negative C_X values mean a net-thrust force on the system.

When the numerical model results are compared with the experimental data, deviations are present, however, the effect of the spanwise propeller position seems to be captured well. The trends are similar between the model and the experiment, which means the most important aerodynamic phenomena are captured. The net-axial force of the system is lower for the tip-mounted configuration compared to the conventional configuration. This difference becomes larger when the lift coefficient and hence the tip vortex strength is increased. This difference in net-axial force is also present in the numerical model. The effect of the difference in propeller trust also seems to be captured well by the numerical model. The differences between the numerical model and the experimental data are primarily present for the higher advance ratios and higher lift coefficients. The deviation at higher lift coefficients is caused by the fact that the numerical model does not include the angle of attack effects on the propeller thrust modeling, hence the net-axial force is increased (in the drag direction).

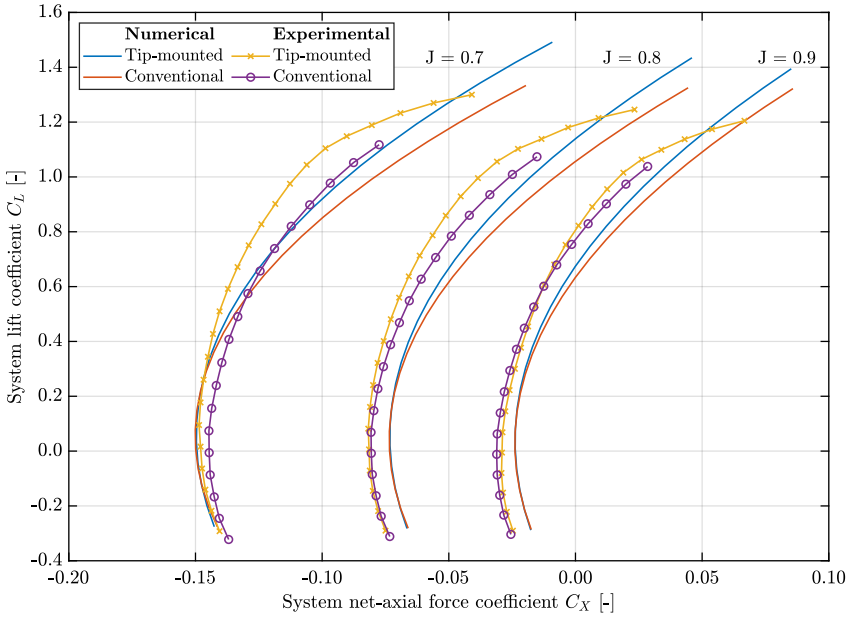

Fig. 9 Aerodynamic polars of the propeller-wing system for a conventional and tip-mounted inboard-up rotating propeller configuration for three different advance ratios

For the higher advance ratios, hence lower thrust settings, there seems to be a constant offset between the model and the experimental data. This is probably caused by an incorrect calculation of the friction drag of the system. It seems that the viscous drag is over-estimated, which causes a shift for all the advance ratios. However, it is known that the used BEM model slightly over-predicts the thrust at lower advance ratios. Therefore, the overestimation in friction drag is canceled again by the over-prediction in thrust for $J = 0.7$. Another reason for this offset could be that the upwash effect of the wing on the propeller performance is not taken into account. This upwash would reduce the local advance ratio and hence increases the thrust on parts of the propeller disk. This disturbed inflow field will affect the propeller performance much more at lower thrust settings than at higher thrust settings. Even though there are some discrepancies between the numerical model and the experiment, the qualitative trends seem to be captured well. Furthermore, this study focuses on the induced drag component only, and the propeller performance and slipstream tube model are merely used as input for the propeller-wing interaction. Another advantage of the numerical model is highlighted by the fact that the lift, vortex-induced drag, and swirl-induced drag can be analyzed separately for multiple propeller-wing system configurations. Instead of having a single system lift and net-axial force, as is the result of the balance measurements in wind tunnel experiments, the induced drag can be decoupled in the numerical model. By this decoupling for different propeller-wing configurations in the parametric study, a better understanding can be obtained of the relation between the induced drag components of the wing.

IV. Results

To investigate the contribution of both the vortex-induced drag and the swirl-induced drag to the total induced drag of the propeller-wing system for different configurations, a parametric study was performed using the numerical model. In this chapter, the results from this parametric study are presented. For all the different configurations tested, the TUD-XPROP propeller geometry was used for the BEM analyses. For the first investigation into the relative importance of the two induced drag mechanisms, the thrust setting was fixed for all analyses. When changing the propeller blade twist and advance ratio, the same thrust coefficient can be achieved at different propeller efficiencies. By varying the efficiency, effectively the amount of swirl is varied. Willemsen [25] investigated the influence of the swirl on the system performance. This analysis concluded that an increase in swirl would lead to an increase in the net swirl recovery effect, but this is reached at a lower propeller efficiency. Since the propeller efficiency is not taken into account in the system performance in the current study, it was chosen that during the analysis, the propeller is operated at the point of maximum propeller efficiency (η_p), such that realistic ratios between propeller axial and tangential velocities are obtained within the propeller slipstream.

As a reference aircraft, the Fokker 50 was used, since it features a simple wing geometry with no quarter chord sweep, and six-bladed unswept propellers, which are similar to the TUD-XPROP. The diameter of the propellers is 3.66 m (12 ft). The spanwise position of the propellers of the Fokker 50 is approximately at $y_p/(b/2) = 0.25$ (3.6 m). The distance between the propeller plane and the leading edge of the wing was estimated to be 2.13 meters. This value was kept constant for all analyses since changing the streamwise distance between the propeller and wing influences the slipstream-induced velocities. The cruise conditions were used for the analyses, and hence the thrust coefficient ($T_C = T/(\rho_\infty V_\infty^2 D_p^2)$) was set to 0.03 [26]. This thrust was achieved by varying the blade pitch setting and the advance ratio to maximize the propeller efficiency in the BEM model. The wing of the Fokker 50 has a taper ratio of 0.4, but for the first analyses using the numerical model, the taper ratio was set to 1, such that there is a constant chord along the span. The detailed inputs used for the numerical model can be found in Table 1. Furthermore, a symmetric airfoil is used over the full span of the wing, leading to a lift curve slope of 2π for all spanwise sections. Note that the analyzed configurations were symmetric with respect to the center of the wing, and hence only one wing half is shown.

Table 1 Input values used during the different analyses

flight conditions			propeller performance			wing planform			
altitude	ρ_∞	V_∞	T_C	J	η_p	b	wing area	sweep	twist
7600 m	0.55 kg/m^3	140 m/s	0.03	2.77	0.86	29 m	70 m^2	0°	0°

The system lift coefficient of the propeller-wing system is fixed at 0.35 during the analyses, such that better insight is obtained into the drag components of the wing during the cruise phase of the aircraft, making the analysis more relevant for aircraft design purposes. In this way, there is also a more fair comparison in terms of induced drag components. Theoretically, if the induced angle of attack distribution would be the same for two different cases, but the integral lift value would be different in some way, there would be also a difference in the integral induced drag, purely due to the difference in resultant force. The desired system lift coefficient is obtained by changing the angle of attack of the wing. As mentioned before, the angle of attack for the propeller performance and slipstream modeling is always set to zero.

A. Variation of Propeller Spanwise Position

From literature, it is known that the spanwise position of the propeller has a significant impact on the performance change of the propeller-wing system. Therefore, two specific propeller positions were analyzed and the wing spanwise loading distributions are investigated to see the effect of the propeller-wing interaction. Hereafter, an analysis is presented where the propeller position is varied along the span of the wing, and the change in integral lift and drag is quantified. Since in these analyses only the induced drag is considered, the subscript i is omitted.

1. Fokker 50 Configuration

As a first analysis, the propeller was placed at the same position as the Fokker 50, but then for the simplified wing geometry. The propeller was set to be rotating inboard-up, and the resulting wing aerodynamic performance distributions are presented in Fig. 10. The sectional lift distribution is shown for a half wing in Fig. 10a, while the sectional drag distribution is shown in Fig. 10b. In both figures, the clean wing distribution is also shown, so without the propeller slipstream influence. For the sectional drag distribution, the total drag is shown, but also the individual components. As mentioned before, the drag component presented is only the induced drag, since the profile drag is omitted. In Fig. 10a, the clean wing spanwise lift distribution is seen by the dashed line. The effects of the propeller slipstream are clearly visible, where the lift at the up-going blade side is increased and at the down-going blade side decreased compared to the clean wing. The positive spanwise lift gradient at the slipstream boundary on the inboard side will cause a decrease in vortex-induced downwash at the root segments, increasing the lift also outside of the propeller slipstream. Note that the lift at the root is also increased due to the influence of the propeller on the other wing half. At the outboard side of the wing, the opposite happens, where the positive spanwise lift gradient at the edge of the slipstream causes additional downwash towards the tip, lowering the lift towards the tip. Another reason that the loading at the tip region is lower, is due to the net lift augmentation effect. To keep the same lift coefficient for the propeller-wing system as for the clean wing, the angle of attack had to be reduced slightly. This lowers the theoretical clean wing lift distribution for this propeller-wing system.

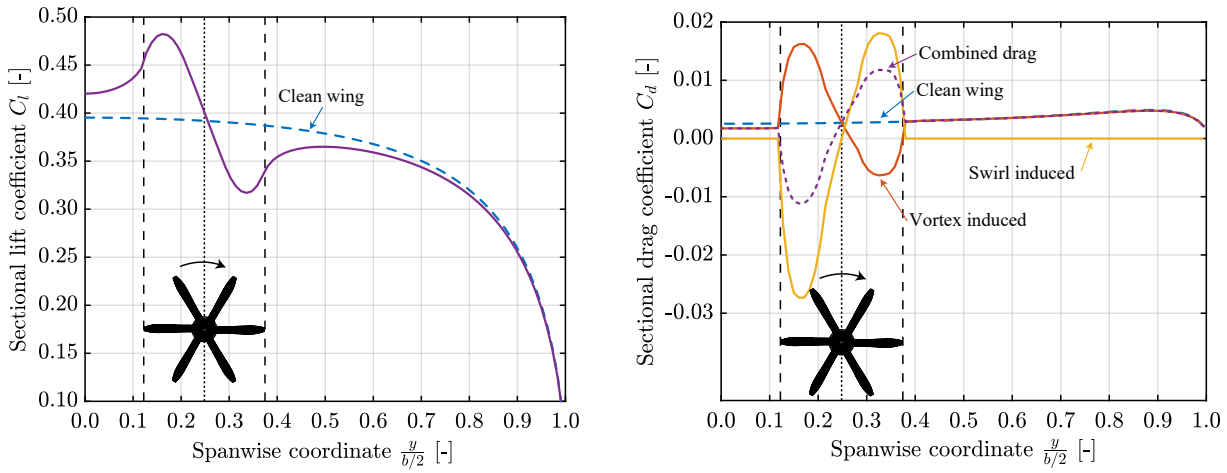

a) Sectional lift distribution **b) Sectional drag distribution for the different components**

Fig. 10 Wing lift and drag distributions for an inboard positioned propeller-wing system

When looking at the sectional drag coefficient in Fig. 10b, the blue dashed line represents the spanwise induced drag distribution of the clean wing. The red line is the spanwise distribution of vortex-induced drag, while the yellow line represents the spanwise swirl-induced drag component. The spanwise distribution of the combined induced drag of the propeller-wing system is shown with the purple dashed line. Since there is no swirl velocity outside of the propeller slipstream, the swirl-induced drag is zero at these segments. At the up-going blade side, the positive swirl velocity results in a negative swirl-induced drag coefficient, meaning a thrust component for the swirl-induced mechanism. However, at the same time, the larger resultant force and the increased vortex-induced downwash at the up-going blade side result in a larger vortex-induced drag. The negative spanwise lift gradient inside the slipstream will cause a decrease in vortex-induced downwash at the down-going blade side, and together with the reduction in the resultant force, the vortex-induced drag is lower compared to the clean wing. The values are even negative for most spanwise segments, meaning there is a net upwash due to the trailing vortex sheet and hence thrust force. However, the propeller-induced downwash makes the swirl-induced component positive, meaning drag at the wing segments behind this side of the propeller.

The net effect of the swirl-induced mechanism for this configuration is a negative drag coefficient because the forward tilting happens at wing segments with a larger resultant force than the backward tilting. Unfortunately, due to the same effect, there is a net increase in vortex-induced drag over the spanwise segments inside the propeller slipstream. When the two effects are summed, the swirl velocity is the most dominant vertical velocity component for this configuration. At the up-going blade side, the swirl-induced drag is larger in magnitude than the increased vortex-induced drag, resulting in a net negative induced drag, meaning a thrust force. At the down-going blade side, the added drag due to the swirl velocity outweighs the decrease in vortex-induced drag, leading to an increase in combined induced drag compared to the clean wing. When the spanwise distributions are integrated over the span, the integral values can be compared, which then includes the change in vortex-induced drag of the spanwise segments outside of the slipstream. These integral values are presented in Sec. IV.A.3. As mentioned before, the large spanwise gradient at the slipstream edges causes a decreased downwash at the root. So even though the lift is much higher than the clean wing at the root segments, the reduction in vortex-induced downwash is larger, reducing the vortex-induced drag. The increased downwash at the outboard region slightly increases the negative induced angle of attack close to the slipstream, but the differences with the clean wing are small. This increase in vortex-induced drag is then offset by a small decrease in vortex-induced drag at the tip region. This comes from the fact that the tip region is not much affected by the propeller slipstream region, but the loading at the tip is smaller than for the prop-off configuration. This is to maintain the integrated lift coefficient at the target value. Next, a tip-mounted propeller-wing configuration is discussed, to see the change in the two drag mechanisms.

2. Tip-Mounted Propeller Configuration

As mentioned in Sec. II.C, the tip-mounted propeller-wing configuration has proved to provide significant performance benefits compared to the more conventional propeller spanwise positions. Therefore, the next analysis was performed using a tip-mounted propeller configuration, while the other input parameters as discussed previously were kept the same, see Table 1. However, for the tip-mounted propeller, half of the slipstream is outside of the wing span. The results in terms of spanwise lift and drag component distribution are shown in Fig. 11 for the tip-mounted propeller configuration. In Fig. 11a and Fig. 11b, the lift and drag distributions are shown, respectively. The sectional lift values of the propeller-influenced wing are significantly different compared to those of the clean wing. This is due to the lift augmentation taking place at the tip, where the loading is low. Furthermore, there is only the increase in lift of the up-going blade side, while the decrease in lift of the down-going blade side is not present. Therefore, the reduction in wing angle of attack to achieve the same integral lift coefficient is larger than for the Fokker 50-like configuration, decreasing the inboard loading.

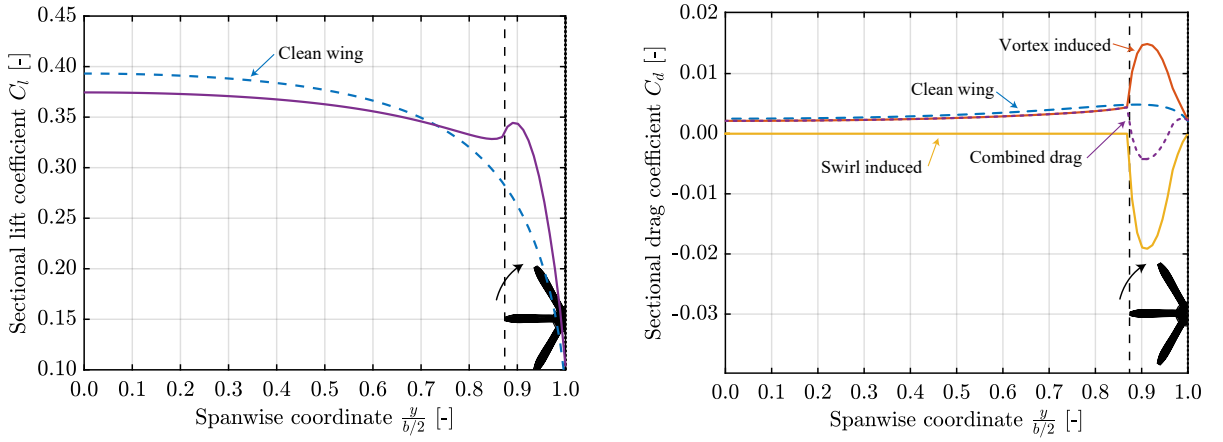

a) Sectional lift distribution **b) Sectional drag distribution for the different components**

Fig. 11 Wing lift and drag distributions for a tip-mounted propeller-wing system

Due to the lift augmentation near the tip, the spanwise lift gradient is smaller over a large part of the wing. However, the spanwise lift gradient is increased in the slipstream region towards the wing tip. This leads to a reduction of vortex-induced drag over a large part of the wing span. The increased vortex-induced downwash in the slipstream and the large increase in local resultant force leads to an increase in vortex-induced drag, while the swirl recovery leads to a drag reduction for the wing segments inside the slipstream. The net effect of the two mechanisms is a large reduction in combined induced drag at the wing tip. In this propeller-wing configuration, the down-rotating side of the propeller is located outside of the span of the wing. This significantly impacts the net beneficial effect of the swirl-induced drag mechanism, which is dominant over the vortex-induced drag mechanism. The integral performance of the tip-mounted configuration is also discussed in the next section.

3. System Performance

To further investigate the effect of the propeller spanwise position on the different drag mechanisms, the integral values of the two different configurations are presented in Table 2. The integral values are obtained by integrating the spanwise loading distributions over the span of the wing. The values were normalized using the clean wing integrated values. This means that the individual drag components of the propeller-wing system are compared to the same value, namely the induced drag of the clean wing. As can be seen, the combined drag of the two different propeller configurations is reduced compared to the clean wing. The reduction in combined drag for $y_p = 0.25\ b/2$ is around 13.6%. However, the tip-mounted case shows a much larger decrease in combined induced drag compared to the clean wing. With a 33.9% reduction in induced drag, the tip-mounted propeller configuration shows its attractiveness compared to the more conventional propeller configuration.

Table 2 Propeller-wing system performance results for the different propeller positions (rotating inboard-up)

		F50	Tip-mounted
Propeller position	y_p	0.25 $b/2$	1.0 $b/2$
Lift coefficient	$C_L/C_{L,clean}$	1.00	1.00
Vortex-induced drag	$C_{D,v}/C_{D,clean}$	1.062	1.107
Swirl-induced drag	$C_{D,s}/C_{D,clean}$	-0.199	-0.446
Combined drag	$C_D/C_{D,clean}$	0.864	0.661

When the individual induced drag mechanisms are investigated, it is confirmed that for the two analyzed configurations, the net swirl-induced drag mechanism inside the propeller slipstream region results in a thrust force. When comparing the integral values of the vortex-induced drag component, it can be seen that both configurations show an increase compared to the clean wing induced drag. This is as expected considering the distortion of the lift distribution introduced by the propeller effect. The biggest increase in the vortex-induced drag is for the tip-mounted configuration, partially offsetting the large negative swirl-induced drag. So even though the increase in vortex-induced drag is larger, the decrease in swirl-induced drag is more dominant, reducing the combined drag of the tip-mounted configuration. It must be noted that these results were all obtained for a wing taper ratio of 1, which means the clean wing spanwise lift distribution has a negative gradient over the whole semi-span. A different taper ratio, hence a different circulation distribution will impact the relative drag reductions obtained for the different propeller spanwise positions. The tip-mounted propeller configuration showed a larger performance enhancement than the conventional configuration. To further investigate the importance of the propeller spanwise position, the spanwise position was varied in a stepwise manner from the root to the tip. In this way, the integral drag components were analyzed for many spanwise propeller positions. In Fig. 12, the results of this analysis are shown, with on the x-axis the propeller position.

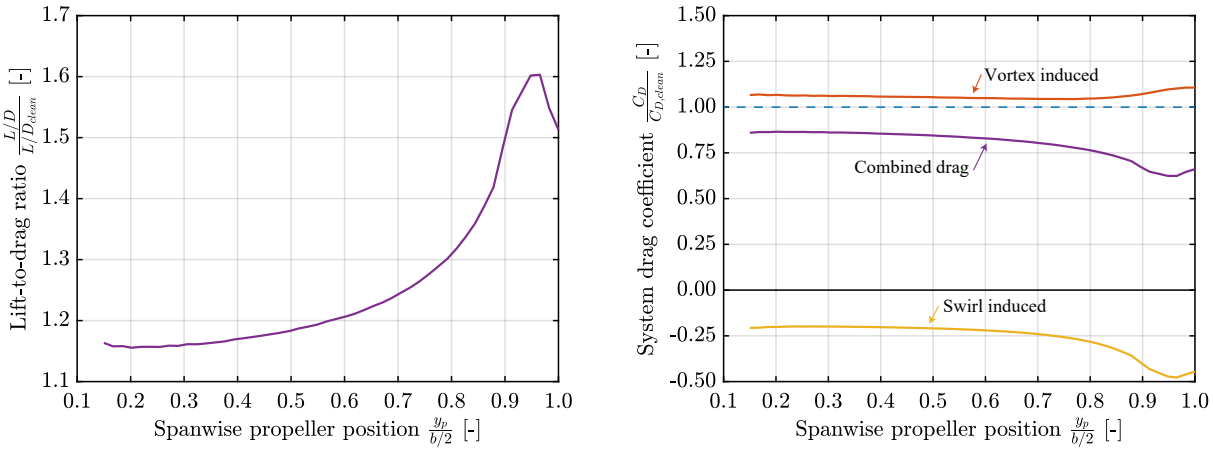

a) Change in wing performance L/D **b) Change in integral wing induced drag components**

Fig. 12 Effect of the propeller spanwise position on the change in integral wing induced drag and L/D compared to the clean wing configuration

In Fig. 12a, the wing aerodynamic performance (in terms of L/D) is compared to that of the clean wing, while in Fig. 12b, the different integral drag values are shown. Note that also for the L/D, only the induced drag is considered. The L/D of the propeller-influenced wing keeps on increasing towards the tip, where also the gradient gets larger. However, it seems there is a peak slightly before the wing tip. At this peak, the increase in L/D is around 60% compared to the clean wing. The magnitude of the gradient of the spanwise lift distribution of the isolated wing increases towards the wingtip, and therefore, the difference between the magnitude of swirl-induced drag component at the wing sections behind the two propeller sides increases, thus the net swirl-induced thrust increases, agreeing with literature [5–7]. The peak in wing performance just before the tip can be clarified when taking a closer look at Fig. 10b, where the

drag contributions of the wing for the more conventional propeller spanwise position are shown. At the center of the slipstream, where the propeller nacelle is located, the axial and tangential induced velocities of the propeller are small, such that they only have a small influence on the spanwise lift and drag distribution of the wing. This also means that the diminishing effects at the down-rotating side are small close to the slipstream center. When the propeller is located slightly more inboard, the swirl-induced drag is further increased in the negative sense, since the resultant force is higher on the wing segments more inboard. So, this increase in negative drag is then larger than the increase in induced drag due to the down-rotating propeller side. When the propeller is located exactly at the tip, the down-rotating propeller is completely outside the span of the wing, but the amount of lift of the wing determining the net swirl recovery of the wing is smaller.

To better understand the relative contribution of the two induced drag mechanisms to the aerodynamic performance enhancement, Fig. 12b can be analyzed. Similar trends as for the L/D can be observed in the swirl-induced drag component. This component becomes more beneficial towards the tip, due to the larger gradients in the lift. Indeed, the swirl-induced thrust force peaks just before the tip, after which it reduces. However, the vortex-induced drag component hardly changes as a function of the propeller spanwise position since the increase compared to the clean wing stays between 4.5% and 10.7% for all spanwise propeller positions. This leads to a total drag reduction trend similar to the swirl recovery trend, confirming its dominance. The vortex-induced drag keeps on increasing along the span and does not feature a peak just before the tip.

B. Propeller Rotational Direction

For the tip-mounted propeller, the rotation direction is of vital importance. Large wing performance benefits can be obtained when having the propeller rotating inboard-up. However, having an opposite rotation direction could potentially lead to large performance degradation, since the down-rotating side will be located at the tip region, while the up-rotating side will be outside of the wing span. To further investigate the importance of the rotation direction, a similar analysis as discussed before was performed, but then with an outboard-up rotation of the propeller. This means that the swirl velocities were inverted on wing segments inside the slipstream. The results in terms of spanwise lift and drag distributions for the two configurations are shown in Fig. 13. The spanwise lift distribution for the Fokker 50-like configuration looks opposite to that of the inboard-up rotating configuration, with a decrease in lift at the inboard part, and an increase in lift on the outboard part, see Fig. 13a. The large negative spanwise lift gradient at the inboard edge of the slipstream creates an additional vortex-induced downwash at the root region, while the negative spanwise gradient at the other slipstream edge creates an induced upwash at the outboard region. This is also visible in the spanwise vortex-induced drag distribution, see Fig. 13b.

The increase in the negative induced angle of attack at the root sections outweighs the decrease in loading, leading to higher vortex-induced drag. Opposite to the inboard-up configuration, the vortex-induced drag at the outboard part is marginally decreased just outside of the slipstream, while further towards the tip the vortex-induced drag is higher, since the loading is higher, due to the increased angle of attack to achieve the same lift coefficient as the clean wing. Since the rotation direction is altered, there will be an overall positive swirl-induced drag together with a negative vortex-induced drag (thrust) at the inboard propeller side. Note that even though the negative swirl-induced drag now is obtained at the lower loaded outboard region, the net swirl-induced effect is still resulting in a thrust force, reducing the wing induced drag. So the initial increase in loading due to the positive swirl velocity on the up-rotating propeller results in more negative swirl-induced drag than the value of positive swirl-induced drag at the down-going blade side.

For the tip-mounted propeller, the situation is different, like for the inboard-up configuration. Now, only the down-rotating propeller side is located in front of the wing, while the up-rotating side is located beyond the wing span. The propeller-induced downwash results in a large drop in lift close to the tip compared to the clean wing, see Fig. 13c. The angle of attack needed to be increased significantly to reach the clean-wing lift coefficient, resulting in higher loading on the inboard wing segments. This also increases the vortex-induced drag on this part of the wing, which is clearly visible in Fig. 13d. Since there is only the propeller-induced downwash, there are large positive swirl-induced drag values at the wing segments immersed in the slipstream, increasing the wing drag. However, due to the lower loading close to the tip, the spanwise lading gradient is reduced here, and this results in a relative vortex-induced upwash, resulting in negative vortex-induced drag values inside the slipstream region. The swirl-induced mechanism is again dominating the vortex-induced mechanism, leading to an increase in combined drag. The integral drag coefficients for the three configurations with outboard-up rotating propellers are shown in Table 3.

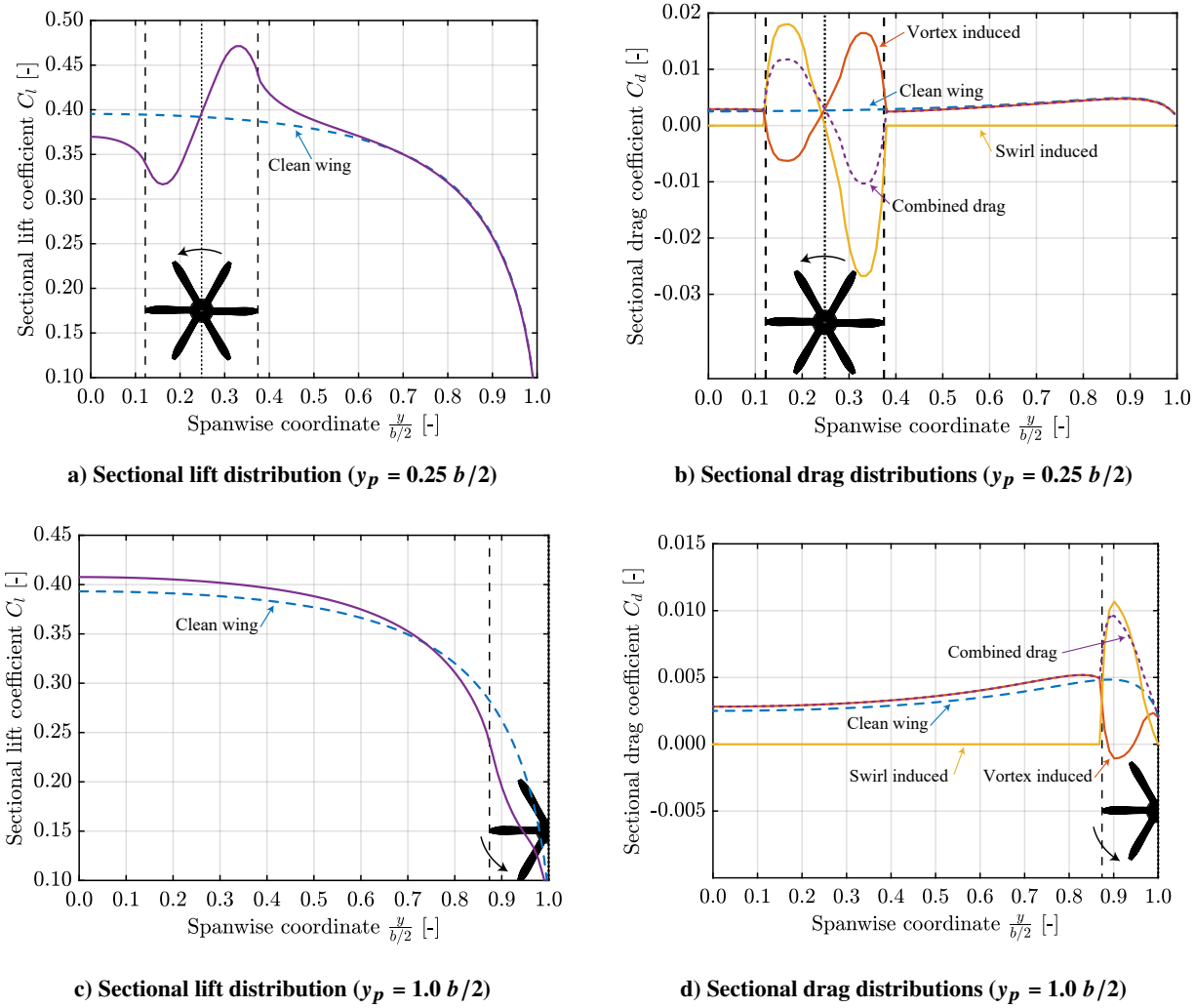

a) Sectional lift distribution (y_p = 0.25 $b/2$)

b) Sectional drag distributions (y_p = 0.25 $b/2$)

c) Sectional lift distribution (y_p = 1.0 $b/2$)

d) Sectional drag distributions (y_p = 1.0 $b/2$)

Fig. 13 Wing lift and drag distributions for the two different propeller-wing systems with outboard-up rotating propellers

Table 3 Propeller-wing system performance results for the different propeller positions (rotating outboard-up)

		F50	Tip-mounted
Propeller position	y_p	0.25 $b/2$	1.0 $b/2$
Lift coefficient	$C_L/C_{L,clean}$	1.00	1.00
Vortex-induced drag	$C_{D,v}/C_{D,clean}$	1.083	0.971
Swirl-induced drag	$C_{D,s}/C_{D,clean}$	-0.187	0.25
Combined drag	$C_D/C_{D,clean}$	0.895	1.218

For the conventional propeller configuration, the integral values reveal an interesting conclusion. The integrated combined drag is still reduced compared to the clean wing. There is a 10.5% reduction in combined drag when the propeller is rotating outboard-up. So even though the propeller rotation direction is changed, there is still an overall reduction in induced drag because the swirl-induced mechanism leads again to a net thrust force, and this is dominant over the increase in vortex-induced drag. However, the total drag reduction is smaller than for the inboard-up rotating cases. The net swirl recovery effect will be largest if the clean wing spanwise lift gradient is smallest, which

is the case for the configuration with $y_p = 0.25\ b/2$. Due to the one-sided slipstream interaction for the tip-mounted propeller configuration, there is a net positive swirl-induced drag coefficient, meaning added induced drag, while the vortex-induced drag coefficient is lower than for the clean wing, due to the large reduction in the slipstream region. Combining the two drag mechanisms, there is a 21.8% increase in combined drag for this configuration.

When the integral aerodynamic performance is to be analyzed for multiple propeller spanwise positions with an outboard-up rotational direction, the trends are different from the inboard-up rotational direction, see Fig 14. The L/D for the outboard-up rotational direction configuration is almost mirrored with respect to the values at the wing root of the inboard-up analysis, see Fig. 14a. So the performance increase compared to the clean wing is almost independent of the rotational direction when the propeller is located close to the root. In both cases, there will be a net swirl recovery effect, leading to a negative integrated swirl-induced drag coefficient, and an increase in vortex-induced drag compared to the clean wing, see Fig. 14b. Similar to the inboard-up rotation case, moving the propeller further towards the wing tip marginally changes the increase in vortex-induced drag compared to the clean wing. The vortex-induced drag increases slightly towards the tip and only when the propeller starts to surpass the wing tip, the vortex-induced drag coefficient drops rapidly. For the swirl-induced drag mechanism, the curve is mirrored with respect to the inboard-up case. The swirl recovery decreases when moving the propeller more outboard since the difference in loading between the two propeller sides becomes increasingly larger. Due to this effect, the combined drag coefficient already becomes larger than the clean wing (1.0) before the propeller starts to surpass the wing tip. Once the propeller slipstream edge is past the wing tip, there is a sharp increase in swirl-induced drag, which is larger than the decrease in vortex-induced drag, meaning the combined drag keeps on increasing further. Eventually, when the spinner region approaches the tip, the two mechanisms become constant in value and so does the combined drag.

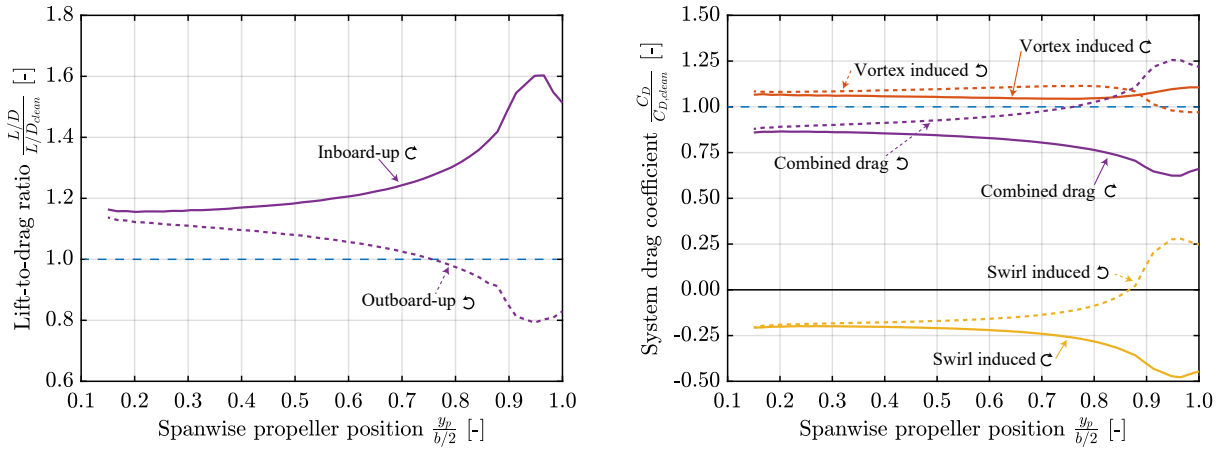

a) Change in wing performance L/D

b) Change in integral wing induced drag components

Fig. 14 Effect of the propeller position on the change in integral wing induced drag and L/D compared to the clean wing configuration for both rotation directions

So when concluding the effects of the rotational direction and propeller position, it can be noted that the largest performance gain, but also the largest performance degradation can be obtained for the propeller located close to the tip, depending on the rotational direction. The more inboard the propeller is placed, the smaller the spanwise loading gradient between the two propeller sides, and hence the lower net swirl-induced effect. This means that the reduction in combined drag is small for the inboard-up rotating configuration, but also it means that there is almost no performance degradation when changing the propeller rotations direction. This also means that when the propellers are to be used for different purposes, e.g. at both positive and negative thrust and power settings, the possible propeller placement should be carefully considered, since the swirl direction will be opposite for the opposite loading. Also for negative thrust and power operations, there will be a reduction in axial-induced velocity, leading to a further increase in vortex-induced drag values.

C. Variation in Taper Ratio

Finally, the effect of changing the wing taper ratio (λ) on the wing performance improvement or degradation was investigated. It was shown that the swirl-induced drag mechanism is influenced by the spanwise loading gradient of the clean wing, hence by changing these gradients at the propeller slipstream region, different performance benefits could be achieved. The loading distribution was altered by varying the taper ratio of the wing while keeping the other input parameters constant and also maintaining the target C_L. In Fig. 15a, the change in the sectional lift distribution of the clean wing can be seen for different taper ratios. The shown taper ratios are 0.1, 0.4, 0.7, and 1.0. The blue line shows the spanwise lift distribution that was used in all previous analyses (λ = 1.0). This clean wing lift distribution contains a negative spanwise gradient over the whole semi-span. When the taper ratio is reduced, the loading becomes increasingly more located at the outboard wing segments, which has two consequences. Firstly, the spanwise loading gradients at the inboard wing segments become positive. The lower the taper ratio, the higher the spanwise loading gradients in the positive sense. Secondly, the spanwise loading gradients at the outboard wing segments will increase in the negative sense due to the outboard shift in peak loading.

When the taper ratio is e.g. 0.7 and the propeller is placed at the Fokker 50 spanwise propeller position (y_p = 0.25 $b/2$), the inboard-up rotating configuration will experience an opposite loading between the two propeller sides, compared to the case where the taper ratio is 1.0. This is similar to the loading conditions for the outboard-up configuration analyzed in Sec. IV.B. For the tip-mounted configuration with an inboard-up rotating propeller, the propeller-induced velocities will further increase the sectional lift close to the wing tip, adding to the negative spanwise loading gradient. In Fig. 15b, the results of the analysis are shown in terms of the integrated combined induced drag of the system, with on the x-axis the taper ratio of the wing. Both the conventional and tip-mounted propeller positions were considered, for both the rotational directions. These integrated drag values were normalized using the clean wing integrated induced drag values.

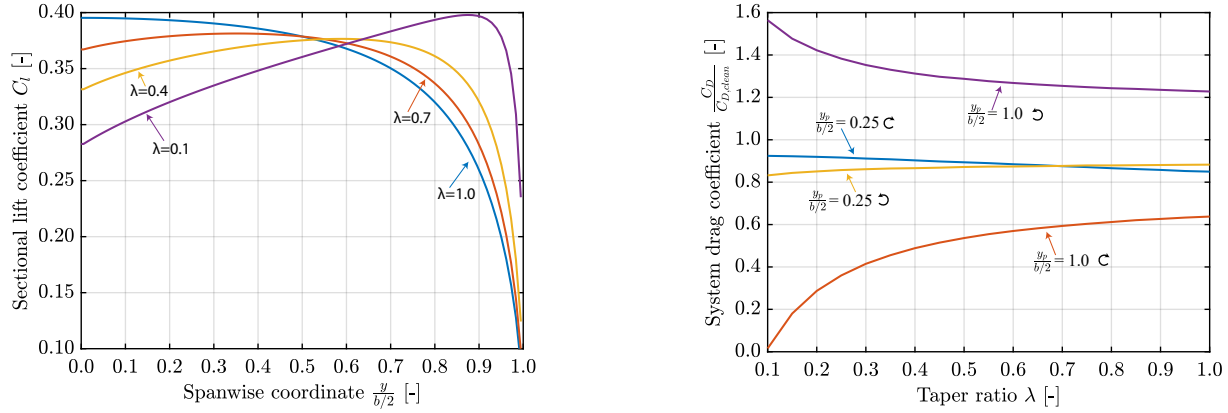

a) Change in the spanwise lift distribution of the clean wing for 4 specific taper ratios

b) Change in integral induced drag for the two propeller spanwise positions and the two rotational directions

Fig. 15 Change in the sectional lift and system induced drag while varying taper ratio (λ)

When decreasing the taper ratio for the conventional position propeller configuration, that is rotating onboard-up (blue line), the reduction in drag becomes smaller. This is due to the spanwise loading gradient that is becoming larger across the propeller slipstream region. Hence, the swirl benefit of the up-going blade side and the down-going blade side becomes smaller. As discussed before, the increase in induced drag due to the vortex-induced mechanism remains more or less constant. So the reduction in the beneficial swirl mechanisms means less induced drag reduction when lowering the taper ratio. When the propeller is rotating outboard-up (yellow line), the drag reduction for λ = 1.0 is indeed smaller than for the inboard-up rotational direction. However, when lowering the taper ratio, the beneficial net swirl effect will increase again, lowering the integrated induced drag of the wing. If a taper ratio of the actual Fokker 50 is analyzed (λ = 0.4), it can be seen that the outboard-up rotational configuration leads to a larger drag reduction than the inboard-up configuration. The gradient at the location of the propeller is positive, such that behind the inboard side of the propeller, the lift of the wing is less compared to the lift behind the outboard side of the propeller. At this propeller spanwise, the difference in lift of the wing behind the two propeller sides is further increased by the outboard-up configuration.

For the tip-mounted configuration, the one-sided propeller interaction makes the net effect of the swirl-induced mechanism much stronger. When the spanwise loading gradient is further increased in magnitude by decreasing the taper ratio, this effect becomes even stronger. For the inboard-up configuration (red line), there is an increase in the drag reduction when lowering the taper ratio. For a Fokker 50-like wing ($\lambda = 0.4$), a tip-mounted propeller would decrease the induced drag of the wing by around 51%, which is more than the value mentioned in Sec. IV.A.2. When the taper ratio is further reduced, the spanwise loading gradients at the wing tip become increasingly larger and so does the swirl-induced mechanism. For the limiting case of $\lambda = 0.1$, the drag reduction would be very large according to the model, almost counteracting the induced drag of the rest of the wing. For the outboard-up configuration (purple line), which already had an increase in drag for the case of $\lambda = 1.0$, the increase in drag becomes even larger when decreasing the taper ratio. It must be noted that the small taper ratio of 0.1 would result in a very small chord at the wing tip segments, being possibly unfeasible for real aircraft designs. Furthermore, placing a large propeller at a tip that is very small would add to the structural complexity of such setups.

V. Conclusions

This study presented a novel way of analyzing the change in induced drag of a propeller-wing system. This was done by considering the individual contribution of the vertical velocity component induced by the trailing vortex sheet, and the vertical velocity component induced by the propeller swirl velocity. For propeller-wing systems, the upwash at the up-going blade side will create a thrust component, a phenomenon known as swirl recovery, which reduces the induced drag. At the same time, the sudden change in the sectional lift at the slipstream-affected region increases the shed vorticity behind the wing resulting in an increased downwash, meaning an increase in induced drag over the complete span. The relative contributions of those two mechanisms to the total induced drag were unknown. A low-order numerical tool was used to split the relative contribution of these two mechanisms. Within the model, both the propeller performance, including the slipstream-induced velocities, and the wing performance, were modeled using potential flow methods. Based on the results from the different analyses, the following conclusions were drawn:

- The net swirl-induced mechanism is a function of the spanwise loading gradients of the clean wing. When the loading at the up-going-blade side is larger than at the down-going blade side, the net swirl-induced mechanism generates an overall negative drag, meaning a thrust component. This is still true when the loading gradient across the slipstream region is opposite in sign but small. When the loading at the up-going blade side becomes too small compared to the down-going blade side, the net effect of the swirl velocity will lead to an increase in swirl-induced drag.
- When the net swirl-induced mechanism creates a thrust force, the vortex-induced mechanism yields a positive induced drag component, meaning it counteracts the beneficial swirl recovery. Also when the swirl-induced drag becomes positive, the vortex-induced drag will become negative. The vortex-induced drag is almost independent of the spanwise loading gradient.
- The swirl-induced drag mechanism is dominant compared to the vortex-induced mechanism. This means that when a net swirl benefit is present (thrust force), it will over-compensate the increase in induced drag due to increased vortex-induced downwash, lowering the combined drag of the system.
- The largest performance gains can be obtained for a tip-mounted propeller configuration, rotating inboard-up. This is due to the large spanwise loading gradients present at the wing tip, together with the fact that only the beneficial swirl side of the propeller is in front of the wing since the down-rotating side is past the wing span.
- For an inboard-up rotating propeller configuration, an overall drag reduction is achieved for inboard propeller positions due to the net beneficial swirl-induced drag. The induced drag will be reduced, independent of the taper ratio and hence the spanwise circulation distribution. Furthermore, the outboard-up rotating configuration will obtain similar drag reduction compared to the inboard-up configurations, at these inboard propeller positions.
- For the outboard-located propeller positions, the change in the rotational direction is detrimental to the wing performance. A tip-mounted propeller configuration will experience a combined induced drag increase for all possible taper ratios when the propeller is rotating outboard-up.
- When the taper ratio is decreased and the spanwise loading gradients at the inboard sections become more and more positive, an outboard-up rotating propeller configuration will yield the largest performance increase.
- Note that all results discussed in this study were obtained with a numerical tool that has certain limitations and shortcomings. Including the viscous effects, also in terms of profile drag, could change the results. Furthermore, the numerical model featured a one-way interaction, so there is no change in propeller and slipstream performance due to the wing-induced velocities. In reality, this effect would again change the wing performance.

The results obtained in this study increase the knowledge regarding the propeller-wing interactions and the change in wing induced drag as a function of the propeller spanwise position and rotational direction. This information can help in the design of novel aircraft using propeller propulsion, as a first estimation of the possible increase in system performance. With this increase in system efficiency, the energy consumption of aircraft can be further reduced, and with that, the impact of aviation on the environment.

Acknowledgments

The research leading to these results is part of the FUTPRINT50 project. This project has received funding from the European Union's Horizon 2020 Research and Innovation programme under Grant Agreement No 875551.

References

[1] J. P. Barnes, "Flight Without Fuel – Regenerative Soaring Feasibility Study," *General Aviation Technology Conference & Exhibition*, 2006. https://doi.org/10.4271/2006-01-2422, Wichita, Kansas.

[2] J. P. Barnes, "Regenerative Electric Flight: Synergy and Integration of Dual-role Machines," *AIAA SciTech Forum;*, Vol. 53rd AIAA Aerospace Sciences Meeting, 2015. https://doi.org/10.2514/6.2015-1302, Kissimmee, Florida.

[3] R. Nederlof, D. Ragni, T. Sinnige, "Experimental Investigation of the Aerodynamic Performance of a Propeller at Positive and Negative Thrust and Power," *AIAA AVIATION Forum;*, 2022. https://doi.org/10.2514/6.2022-3893, Chicago, Illinois.

[4] L. L. M. Veldhuis, "Propeller Wing Aerodynamic Interference," Ph.D. thesis, Faculty of Aerospace Engineering, Delft University of Technology, Delft, The Netherlands, 2005.

[5] D. P. Witkowski, A. K. H. Lee, and J.P. Sullivan, "Aerodynamic Interaction Between Propellers and Wings," *Journal of Aircraft*, Vol. 26, No. 9, 1989, pp. 829–836. https://doi.org/10.2514/3.45848.

[6] I. Kroo, "Propeller-wing integration for minimum induced loss," *Journal of Aircraft*, Vol. 23, No. 7, 1986, pp. 561–565. https://doi.org/10.2514/3.45344.

[7] M. H. Snyder and G. W. Zumwalt, "Effects of Wingtip- Mounted Propellers on Wing Lift and Induced Drag," *Journal of Aircraft*, Vol. 6, No. 5, 1969, pp. 392–397. https://doi.org/10.2514/3.44076.

[8] J. L. Loth and F. Loth, "Induced Drag Reduction With Wing Tip Mounted Propellers," *2nd Applied Aerodynamics Conference*, 1984. https://doi.org/10.2514/6.1984-2149, Seattle, Washington.

[9] T. Sinnige, N. van Arnhem, T. C. A. Stokkermans, G. Eitelberg and L. L. M. Veldhuis, "Wingtip-Mounted Propellers: Aerodynamic Analysis of Interaction Effects and Comparison with Conventional Layout," *Journal of Aircraft*, Vol. 56, No. 1, 2019, pp. 295–312. https://doi.org/10.2514/1.C034978.

[10] N. van Arnhem, T. Sinnige, T. C. A. Stokkermans, G. Eitelberg and L. L. M. Veldhuis, "Aerodynamic Interaction Effects of Tip-Mounted Propellers Installed on the Horizontal Tailplane," *2018 AIAA Aerospace Sciences Meeting*, 2018. https://doi.org/10.2514/6.2018-2052, Kissimmee, Florida.

[11] T. Sinnige, R. Nederlof and N. van Arnhem, "Aerodynamic Performance of Wingtip-Mounted Propellers in Tractor and Pusher Configuration," *AIAA AVIATION Forum, Virtual Event*, 2021. https://doi.org/10.2514/6.2021-2511.

[12] J. R. Hooker, A. T. Wick, J. Walker and B. T. Schiltgen, "Overview of Low Speed Wind Tunnel Testing Conducted on a Wingtip Mounted Propeller for the Workshop for Integrated Propeller Prediction," *AIAA AVIATION Forum*, 2020. https://doi.org/10.2514/6.2020-2673, Virtual Event.

[13] O. Pfeifle, S. Notter, W. Fichter, D. P. Bergmann, J. Denzel and A. Strohmayer, "Verifying the Effect of Wingtip Propellers on Drag Through In-Flight Measurements," *Journal of Aircraft*, Vol. 59, No. 2, 2022, pp. 474–483. https://doi.org/10.2514/1.C036490.

[14] M. Schollenberger, T. Lutz, D.P. Bergmann and A. Strohmayer, "Numerical investigation of the influence of geometric and operational parameters on the aerodynamic interactions of wingtip mounted propellers," *AIAA AVIATION Forum*, 2022. https://doi.org/10.2514/6.2022-3300, Chicago, Illinois.

[15] J. A. Cole, T. Krebs, D. Barcelos and G. Bramesfeld, "Influence of Propeller Location, Diameter, and Rotation Direction on Aerodynamic Efficiency," *Journal of Aircraft*, Vol. 58, No. 1, 2021, pp. 63–71. https://doi.org/10.2514/1.C035917.

[16] R. T. Johnston, and J. P. Sullivan, "Unsteady Wing Surface Pressures in the Wake of a Propeller," *Journal of Aircraft*, Vol. 30, No. 5, 1993, pp. 644–651. https://doi.org/10.2514/3.46393.

[17] T. Sinnige, R. de Vries, B. Della Corte, F. Avallone, D. Ragni, G. Eitelberg, and L. L. M. Veldhuis, "Unsteady Pylon Loading Caused by Propeller-Slipstream Impingement for Tip-Mounted Propellers," *Journal of Aircraft*, Vol. 55, No. 4, 2018, pp. 1605–1618. https://doi.org/10.2514/1.C034696.

[18] M. Drela, "QPROP Formulation," https://web.mit.edu/drela/Public/web/qprop/qprop_theory.pdf, 2006.

[19] Q. Li, K. Öztürk, T. Sinnige, D. Ragni, Y. Wang, G. Eitelberg and L. L. M. Veldhuis, "Design and Experimental Validation of Swirl Recovery Vanes for Propeller Propulsion Systems," *AIAA Journal*, Vol. 56, No. 12, 2018, pp. 4719–4729. https://doi.org/10.2514/1.J057113.

[20] J. Goyal, T. Sinnige, F. Avallone and C. Ferreira, "Aerodynamic and Aeroacoustic Characteristics of an Isolated Propeller at Positive and Negative Thrust," *AIAA AVIATION Forum;*, 2021. https://doi.org/10.2514/6.2021-2187.

[21] W. F. Phillips and D. O. Snyder, "Modern Adaptation of Prandtl's Classic Lifting-Line Theory," *Journal of Aircraft*, Vol. 37, No. 4, 2000, pp. 662–670. https://doi.org/10.2514/2.2649.

[22] J. Weissinger, "The Lift Distribution of Swept-Back Wings," TM-1120, NACA, 1947.

[23] S. Rethorst, "Aerodynamic of Nonuniform Flows as Related to an Airfoil Extending Through a Circular Jet," *Journal of the Aerospace Sciences*, Vol. 25, No. 1, 1958, pp. 11–28. https://doi.org/10.2514/8.7479.

[24] R. Nederlof, "Improved modeling of propeller-wing interactions with a lifting-line approach: Investigation of a suitable correction method to account for the finite slipstream height," Msc thesis, Delft University of Technology, 2020.

[25] R. Willemsen, "A sensitivity study on the aerodynamic performance of a wingtip-mounted tractor propeller-wing system," Msc thesis, Delft University of Technology, 2020.

[26] P. C. M. van den Borne and J. van Hengst, "Investigation of Propeller Slipstream Effects on the Fokker 50 Through In-Flight Pressure Measurements," *Flight Simulation Technologies Conference and Exhibit*, 1990. https://doi.org/10.2514/6.1990-3084, Dayton, Ohio.